Article

A Structural Comparison of Oral SARS-CoV-2 Drug Candidate Ibuzatrelvir Complexed with the Main Protease (M^pro) of SARS-CoV-2 and MERS-CoV

Pu Chen, Tayla J. Van Oers, Elena Arutyunova, Conrad Fischer, Chaoxiang Wang, Tess Lamer, Marco J. van Belkum, Howard S. Young, John C. Vederas,* and M. Joanne Lemieux*
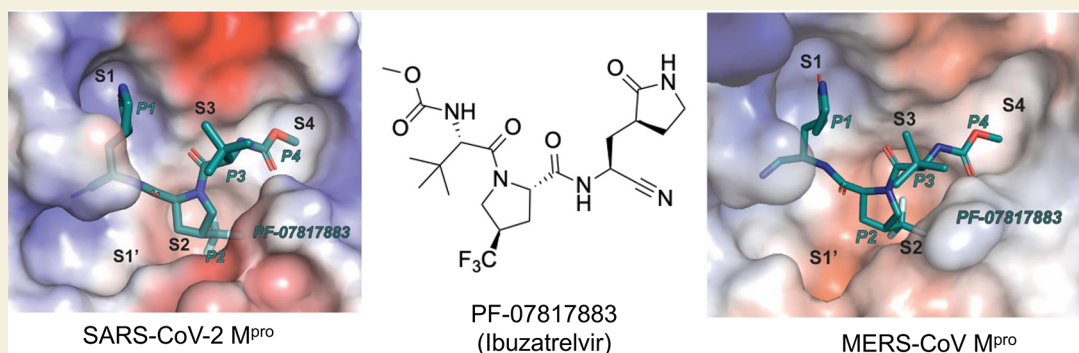
Cite This: *JACS Au* 2024, 4, 3217−3227

Read Online

ACCESS | Metrics & More | Article Recommendations | Supporting Information

SARS-CoV-2 M^pro   PF-07817883 (Ibuzatrelvir)   MERS-CoV M^pro

ABSTRACT: Ibuzatrelvir (1) was recently disclosed and patented by Pfizer for the treatment of severe acute respiratory syndrome coronavirus 2 (SARS-CoV-2). It has received fast-track status from the USA Food and Drug Administration (FDA) and has entered phase III clinical trials as a possible replacement for Paxlovid. Like nirmatrelvir (2) in Paxlovid, this orally active drug candidate is designed to target viral main proteases (M^pro) through reversible covalent interaction of its nitrile warhead with the active site thiol of the chymotrypsin-like cysteine protease (3CL protease). Inhibition of M^pro hinders the processing of the proteins essential for viral replication *in vivo*. However, ibuzatrelvir apparently does not require ritonavir (3), which is coadministered in Paxlovid to block human oxidative metabolism of nirmatrelvir. Here, we report the crystal structure of the complex of ibuzatrelvir with the active site of SARS-CoV-2 M^pro at 2.0 Å resolution. In addition, we show that ibuzatrelvir also potently inhibits the M^pro of Middle East respiratory syndrome-related coronavirus (MERS-CoV), which is fortunately not widespread but can be dangerously lethal (∼36% mortality). Co-crystal structures show that the binding mode of the drug to both active sites is similar and that the trifluoromethyl group of the inhibitor fits precisely into a critical S2 substrate binding pocket of the main proteases. However, our results also provide a rationale for the differences in potency of ibuzatrelvir for these two proteases due to minor differences in the substrate preferences leading to a weaker H-bond network in MERS-CoV M^pro. In addition, we examined the reversibility of compound binding to both proteases, which is an important parameter in reducing off-target effects as well as the potential immunogenicity. The crystal structures of the ibuzatrelvir complexes with M^pro of SARS-CoV-2 and of MERS-CoV will further assist drug design for coronaviral infections in humans and animals.

KEYWORDS: 3CL protease, ibuzatrelvir, antivirals, SARS-CoV-2, COVID, crystallography

■ INTRODUCTION

Significant endeavors have been dedicated to developing antiviral medications during the SARS-CoV-2 pandemic as well as past outbreaks of severe acute respiratory syndrome coronavirus (SARS-CoV) and Middle East respiratory syndrome-related coronavirus (MERS-CoV). Since then, only a small number of medications have been approved by the FDA, including Paxlovid (ritonavir-boosted nirmatrelvir)[1] targeting the SARS-CoV-2 main protease (M^pro, also known as 3CL^pro), and remdesivir, targeting the SARS-CoV-2 RNA-dependent RNA polymerase (RdRp).[2] Moreover, certain

treatments have been approved regionally or conditionally while some are in different phases of clinical trials.[3−8]
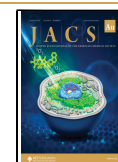
M^pro, a cysteine protease, is an essential enzyme that cleaves 11 sites of the two coronavirus polyproteins pp1a and pp1ab to
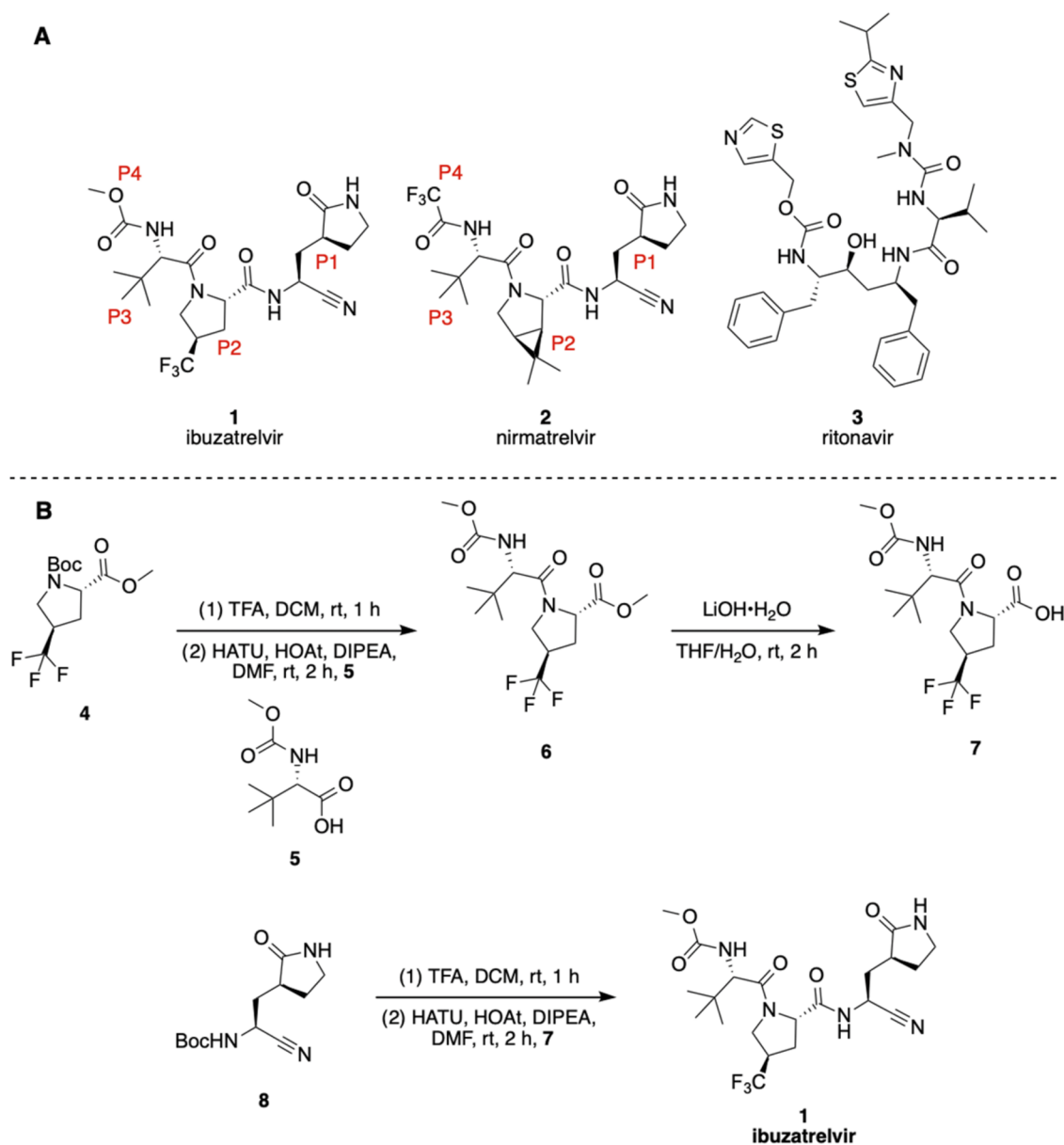
3217

Figure 1. (A) Structures of ibuzatrelvir, nirmatrelvir, and ritonavir. The P1 residue sits in the S1 binding pocket of the enzyme active site, the P2 residue in the S2 pocket, etc. (B) Synthetic route to ibuzatrelvir (1) using solution phase peptide coupling methods.

produce mature proteins that are required for viral replication.[9,10] Moreover, M[pro] shows lower variability among SARS-CoV-2 variants in comparison to other viral proteins, especially at the catalytic site, which has a common catalytic dyad of cysteine-histidine (Cys145-His41), making it a promising target for therapeutic development. Nirmatrelvir (Figure 1A), a component of Paxlovid, is a peptidomimetic SARS-CoV-2 M[pro] inhibitor that forms a reversible covalent bond with Cys145.[1,11] Ritonavir (Figure 1A), the second component of Paxlovid, acts as a pharmacokinetic booster by inhibiting human cytochrome P450 3A4 (CYP 3A4), which is responsible for the metabolism of approximately 50% of all therapeutics.[12,13] However, ritonavir is less compatible with some patients due to drug contraindications.[12] Therefore, a single-agent orally active SARS-CoV-2 M[pro] inhibitor is highly desirable.

Pfizer announced a second-generation SARS-CoV-2 M[pro] drug candidate, ibuzatrelvir (PF-07817883) (Figure 1A), which has a fast-track status and is reported to have successfully completed Phase 2 clinical trials.[14] It is more metabolically stable and has fewer potential drug−drug interactions. Remarkably, no pharmacokinetic booster is required to maintain the drug concentration in plasma.

Ibuzatrelvir, similar to nirmatrelvir, contains an electrophilic nitrile warhead for covalent interaction with the thiol of M[pro] catalytic cysteine. There are several crystal structures of nitrile warheads in complex with the SARS-CoV-2 M[pro] from us and other groups.[3,15−19] The SARS-CoV-2 M[pro] has also been crystallized in complex with many different covalent inhibitors containing a variety of warhead functional groups.[16,20] For example, a ketoamide compound was shown bound in the active site from the group of Hilgenfeld,[21] and we reported a crystal structure of the SARS-CoV-2 M[pro] with GC373, an aldehyde.[10] Our interest in the SARS-CoV-2 main protease and its inhibitors[22−24] prompted us to examine how ibuzatrelvir inhibits SARS-CoV-2 M[pro] in vitro and explore its
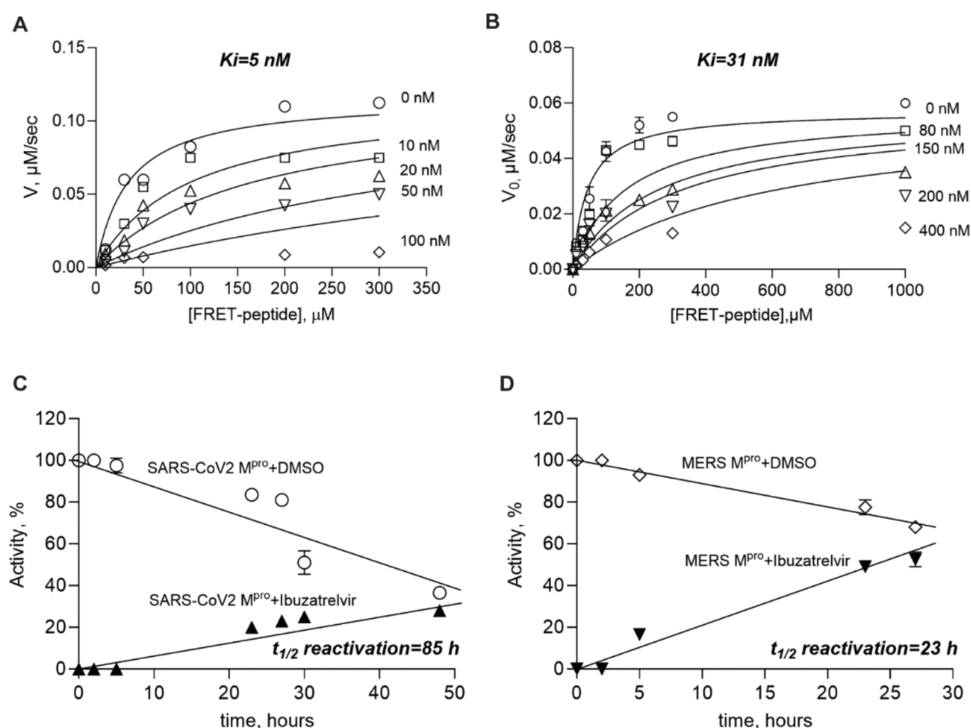
Figure 2. K_i values determination of ibuzatrelvir for SARS-CoV-2 M^pro (A) and MERS-CoV M^pro (B). Purified enzymes were incubated with increasing concentrations of FRET substrate in the absence (0 nM) or presence of different concentrations (10−400 nM) of ibuzatrelvir. Data represent mean ± SEM of 2 independent experiments performed in duplicate. Time course of regained activity of SARS-CoV-2 M^pro (C) and MERS-CoV (D) after being incubated with 20 μM ibuzatrelvir, DMSO was used as a negative control for both proteases.

interaction with the M^pro of another coronavirus, MERS-CoV. We now report and compare binding parameters and crystal structures of M^pro from SARS-CoV-2 and MERS-CoV in complex with ibuzatrelvir.

■ RESULTS

Ibuzatrelvir (**1**) was synthesized via a slightly modified convergent route (Figure 1B), as opposed to the reported procedure, which describes a linear sequence of steps. This was done to conserve the key trifluoromethyl proline building block, which is expensive and difficult to prepare synthetically.[25] The protected amino acid building blocks were prepared according to literature procedures.[26] The tripeptide was assembled by first coupling the *tert*-butyl glycine (**5**) and trifluoromethyl proline (**4**) residues, followed by deprotection of proline C-terminal methyl ester **6**. The free dipeptide acid **7** was then coupled to the cyclic glutamine nitrile **8**. This route limits the number of steps after incorporation of the key trifluoromethyl proline residue to conserve this material. The final compound **1** was isolated as a mixture of diastereomers, which were separated with reverse-phase high-performance liquid chromatography (HPLC) (Figure S7). Separation of the diastereomers was not required for X-ray crystallography, as incubation of this mixture with either SARS-CoV-2 or MERS-CoV main proteases allowed us to obtain X-ray crystal structures of these enzymes covalently bound to the active diastereomer of the inhibitor. The identity and stereochemical purity at each residue were confirmed by acidic hydrolysis, derivatization to *N*-pentafluoropropanide methyl esters, and gas chromatography−mass spectrometry (GC-MS) analysis using a chiral phase column (Supporting Information). Each diastereomer exists as a mixture of interconverting conformers at 20 °C based on ^{1}H and ^{19}F NMR analyses (see the

Supporting Information), but coalescence of signals occurs upon heating at 55 °C, indicating that the conformers are *cis* and *trans* isomers of the proline amide bond.[27]

As shown in Figure 1A, ibuzatrelvir shares some chemical features with nirmatrelvir, and both inhibitors mimic the sequence of the natural substrate of SARS-CoV-2 M^pro. When protease substrate sequences are examined, by convention, P1 is the position of the peptide substrate immediately N-terminal to the scissile amide bond, P2 is N-terminal to P1, and so on. The preferred substrate (consensus sequence) of the SARS-CoV-2 M^pro contains a glutamine in P1, a leucine in P2, and then P3 and P4 have more variability in tolerated residues. Inhibitors nirmatrelvir and ibuzatrelvir both contain a cyclic glutamine lactam in P1 as an analogue of the important glutamine residue of the consensus sequence.[9,10] Both inhibitors also have bulky hydrophobic residues at P2 and P3, with P2 being an analogue of leucine in both cases. Although nirmatrelvir has a bicyclic leucine analogue, ibuzatrelvir incorporates a trifluoromethyl proline residue. Finally, the capping group at P4 was changed from trifluoroacetamide in nirmatrelvir to methyl carbamate in ibuzatrelvir, which has a smaller alanine-like assembly in SARS-CoV-2 M^pro at the S4 pocket.

As reported, ibuzatrelvir is a potent inhibitor of SARS-CoV-2 M^pro.[14] We determined IC$_{50}$ and K_i values for SARS-CoV-2 M^pro being 19 and 5 nM, respectively. The potency of ibuzatrelvir for MERS-CoV M^pro was less with an IC$_{50}$ value of 65 nM and a K_i value of 31 nM (Figure 2A,B and Table 1). A very recent Pfizer publication reported the corresponding values (K_i of 2.48 nM for the SARS-CoV-2 M^pro) and (IC$_{50}$ of 930 nM for the MERS-CoV M^pro) using a different FRET substrate.[14]

Table 1. IC$_{50}$ Values of Ibuzatrelvir for Different M^{pro} Enzymes[a]

protein	IC$_{50}$ (ibuzatrelvir, nM)
SARS-CoV-2 M^{pro}	19 ± 4
MERS-CoV M^{pro}	65 ± 10
SARS-CoV-2 M^{pro} P132H	13 ± 3
SARS-CoV-2 M^{pro} L50F	6 ± 0.5
SARS-CoV-2 M^{pro} T190I	52 ± 12
SARS-CoV-2 M^{pro} E47N	55 ± 15
SARS-CoV-2 M^{pro} E47K	22 ± 2
SARS-CoV-2 M^{pro} S46F	16 ± 3

[a]Data represents mean ± SEM of 2 independent experiments.

To shed light on the mode of binding of ibuzatrelvir to the active site of viral main proteases, we crystallized the inhibitor with SARS-CoV-2 M^{pro} and with MERS-CoV M^{pro}. The structure of the protein-inhibitor complex was determined at 2.0 Å resolution for SARS-CoV-2 M^{pro} and 1.5 Å resolution for MERS-CoV M^{pro}. The asymmetric unit of the complex of SARS-CoV-2 M^{pro} with ibuzatrelvir contained two chains (Figure S1A), forming a dimer, whereas for the MERS-CoV, M^{pro}-ibuzatrelvir complex revealed a single chain. The physiological dimer of the latter complex was generated by PISA program (Figure S1B).[28]

Similar to nirmatrelvir, ibuzatrelvir binds covalently to the active site of SARS-CoV-2 M^{pro}, generating a thioimidate adduct via the attack of Cys145 thiol on the nitrile warhead, forming a covalent bond of 1.77 Å (Figures 3A and 4A). The P1 lactam group is stabilized in the S1 pocket by interactions between the nitrogen atom of the lactam ring and side chains of Phe140 and Glu166. The Ser1 from the other protomer coordinates the network by additional hydrogen bonding interactions with these two residues (Phe140 and Glu166), similar to other structures.[23] The oxygen of the P1 lactam interacts with the side chain of His163 via a hydrogen bond at 2.7 Å (Figure 3A). This network efficiently orients the P1 lactam into the S1 pocket. The ibuzatrelvir binding pattern is nearly identical in the S1 pocket of MERS-CoV M^{pro}, which is not surprising given the high degree of conservation across active site residues between the two main proteases (Figure 4A). However, Ser1 from the neighboring protomer forms longer-length hydrogen bonds with Phe143 and Glu169 in MERS-CoV M^{pro} compared to those in SARS-CoV-2 M^{pro}. This indicates a weaker interaction of the protomers in MERS-CoV M^{pro} because this network contributes to the dimerization in both M^{pro} enzymes (Figures 3A and 4A).

Alterations in the P2 position of ibuzatrelvir compared to nirmatrelvir enhance the binding efficiency into the S2 pocket in both M^{pro} enzymes from SARS-CoV-2 and MERS-CoV.
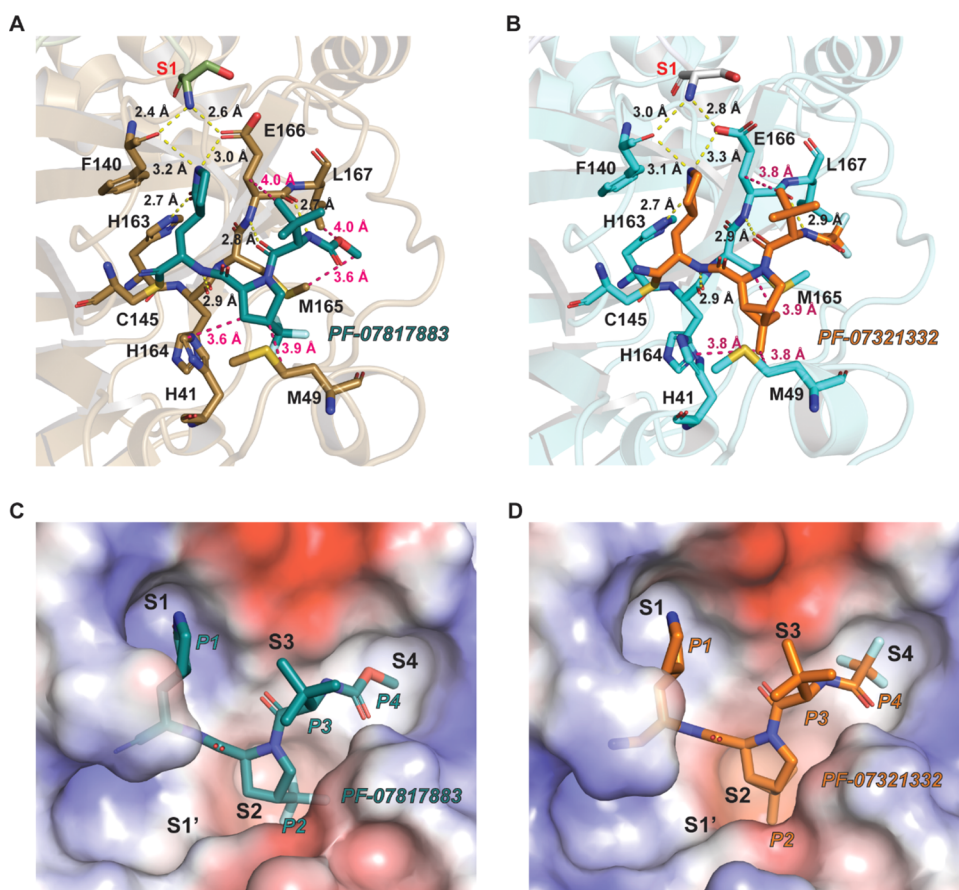

Figure 3. Structural comparison of the SARS-CoV-2 main protease in complex with ibuzatrelvir (PF-07817883) and nirmatrelvir (PF-07321332). The hydrogen bonds and hydrophobic interactions between M^{pro} and ibuzatrelvir (A) or nirmatrelvir (B, PDB entry 7RFS), respectively, are shown. Electrostatic potential surfaces of M^{pro} around the ibuzatrelvir binding site (C) or nirmatrelvir binding site (D) are given below. Ibuzatrelvir and nirmatrelvir are shown as sticks, hydrogen bonds are shown as yellow dashes and labeled with distances, and hydrogen interactions are indicated with hot pink dashes and labeled with distances between carbon atoms. M^{pro} substrate binding pockets are labeled as S1′, S1, S2, S3, and S4, and the corresponding inhibitor chemical groups are labeled as P1, P2, P3, and P4, respectively.
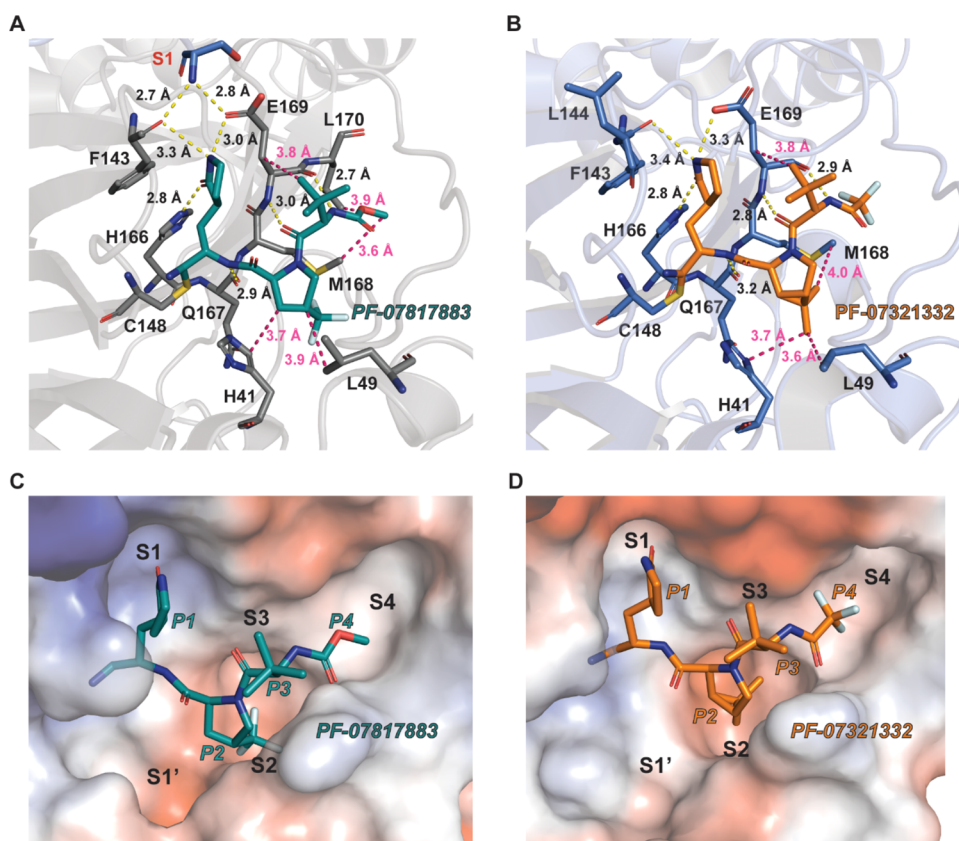
Figure 4. Structural comparison of MERS-CoV M^pro in complex with ibuzatrelvir (PF-07817883) and nirmatrelvir (PF-07321332). The hydrogen bonds and hydrophobic interactions between M^pro and ibuzatrelvir (A) or nirmatrelvir (B) (PDB: 7VTC), respectively. Electrostatic potential surface of M^pro around ibuzatrelvir binding site (C) or nirmatrelvir binding site (D). Ibuzatrelvir and nirmatrelvir are shown as sticks, hydrogen bonds are shown as yellow dashes and labeled with distances, and hydrogen interactions are indicated with hot pink dashes and labeled with distances between carbon atoms. M^pro substrate binding pockets are labeled as S1′, S1, S2, S3, and S4, and the corresponding inhibitor chemical groups are labeled as P1, P2, P3, and P4 respectively.

Compared to the bicyclic leucine mimic of nirmatrelvir, the trifluoromethyl proline derivative provides increased solubility and less restricted rotation around the P2/P3 amide bond. Despite the electronegativity of the CF_3 group, it still fits into the negatively charged S2 pocket of the active site efficiently. The P2 group is stabilized by hydrophobic interactions with the S2 pocket where the β-carbon of the five-membered proline ring forms a CH−π interaction with His41, and the γ-carbon is involved in the hydrophobic interface with the side chain of Met49 (Figure 3A,C). Analogously, Leu49 in the S2 pocket of MERS-CoV M^pro maintains the hydrophobic interaction with the P2 proline-like ring (Figure 4A,C). In the case of nirmatrelvir in complex with SARS-CoV-2 M^pro, a CH_3 of the P2 moiety hydrophobically interacts with His41 and Met49, while the other CH_3 group is close to Met165 at 3.9 Å (Figure 3B). Similar hydrophobic interactions have been found in the MERS-CoV M^pro-nirmatrelvir complex (Figure 4B). Overall, in the S2 pocket of both proteases, the hydrophobic interactions are the main driving forces of binding for both nirmatrelvir and ibuzatrelvir. With nirmatrelvir, the proper positioning of P2 is maintained despite negligible electrostatic interactions with the S2 region (Figures 3D and 4D).

The *tert*-butyl substituent at P3 is present in both ibuzatrelvir and nirmatrelvir and shows essentially the same binding pattern in both cases (Figures 3A,B and 4A,B). The distinctive feature of the S3 sites of both SARS-CoV-2 and

MERS-CoV main proteases is that they are quite open and able to accept large residues (Figures 3C and 4C). As shown in Figure 3A, a CH_3 group at the P3 position of ibuzatrelvir is interacting hydrophobically with the side chain of Glu166 (Glu169 for MERS-CoV M^pro, Figure 4A) while the backbone of ibuzatrelvir forms two hydrogen bonds with Glu166 at 2.8 and 2.7 Å, respectively. The corresponding hydrogen bonds are 3.0 and 2.7 Å in MERS-CoV M^pro (Figure 4A), demonstrating a weaker interaction. With nirmatrelvir, similar interactions were present, but since the distances are ~2.9 Å for both hydrogen bonds in both enzymes, they may be slightly weaker (Figures 3B and 4B).

The trifluoroacetamide capping group of nirmatrelvir is replaced with a methyl carbamate as the P4 capping group in ibuzatrelvir, which is smaller, more hydrophobic, and possibly more favored by the S4 pocket of SARS-CoV-2 M^pro. The CH_3 moiety is surrounded by two residues, Met165 and Leu167, which generate tight hydrophobic interactions (Figure 3A,C). The conserved residues in the MERS-CoV M^pro (Met168 and Leu170) interact with the ibuzatrelvir capping group in a similar fashion (Figure 4A). The trifluoroacetamide capping group of nirmatrelvir fits well into the S4 pocket of both M^pro enzymes. Notably, Met165 of SARS-CoV-2 M^pro interacts with a methyl group of the P2 bicyclic leucine of nirmatrelvir (Figure 3B) (Met168 for the MERS-CoV M^pro) (Figure 4B). However, alternatively, with ibuzatrelvir, this Met residue forms a strong hydrophobic interaction with the P4 group
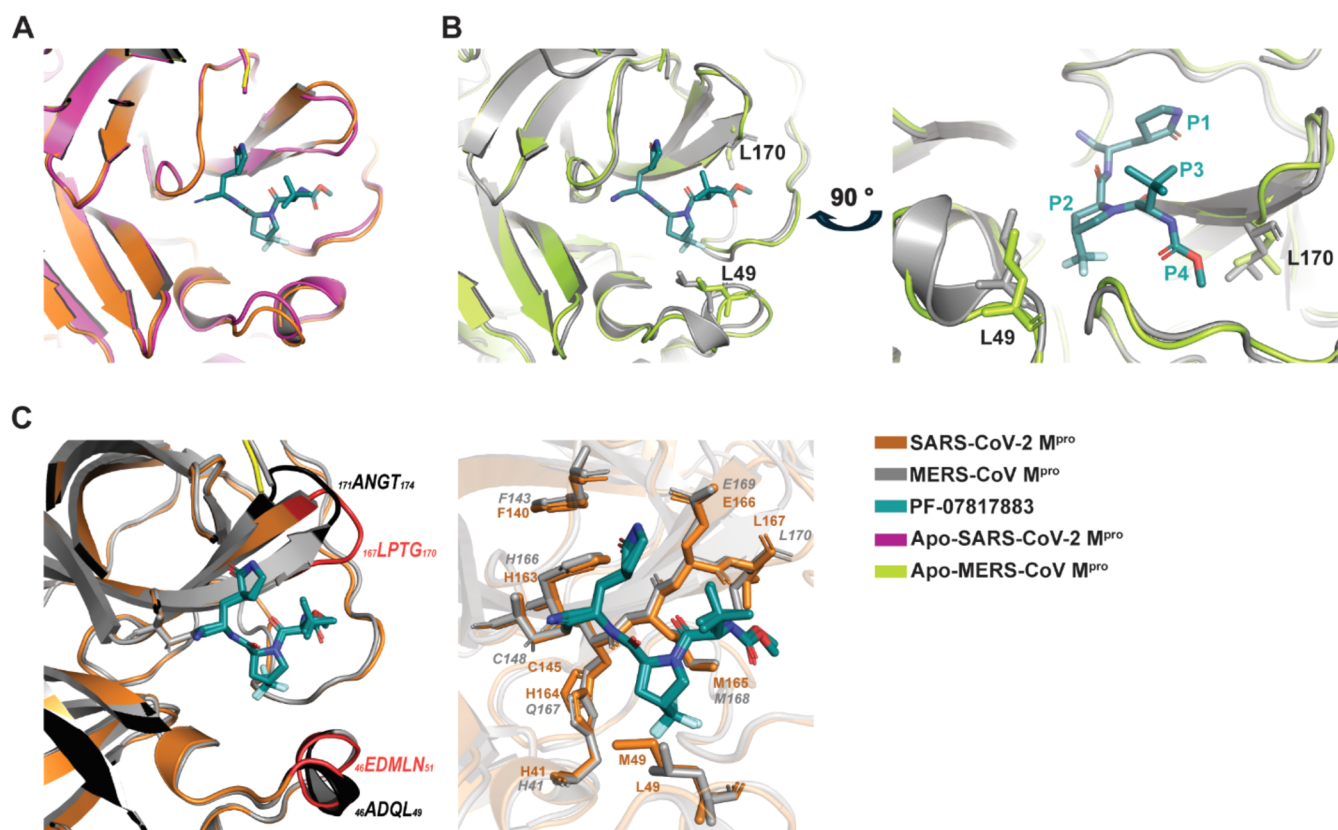
Figure 5. (A) Structural alignment of SARS-CoV-2 M^{pro} in complex with ibuzatrelvir and apo SARS-CoV-2 M^{pro} (PDB: 6WTM). (B) Structural alignment of MERS-CoV M^{pro} in complex with ibuzatrelvir and apo-MERS-CoV M^{pro} (PDB: 5C3N); ibuzatrelvir induced the confirmation change in MERS-CoV M^{pro} via hydrophobic interactions between the P4 group and Leu170. (C) Structural alignment of complexes of ibuzatrelvir with main proteases of SARS-CoV-2 and MERS-CoV.

(Figures 3A and 4A). Thus, this methyl carbamate of ibuzatrelvir at P4 improves the precision of binding compared to the trifluoroacetamide group of nirmatrelvir.

Residues involved in the ibuzatrelvir interaction with SARS-CoV-2 M^{pro} are highly conserved in MERS-CoV M^{pro} (Figure 5C, right). However, the S4 pocket of MERS-CoV M^{pro} is larger because the loop ($_{167}$LPTG$_{170}$) of SARS-CoV-2 M^{pro} is closer to the α-helix ($_{46}$EDMLN$_{51}$) compared to the corresponding distance between the loop ($_{171}$ANGT$_{174}$) and the α-helix ($_{46}$ADQL$_{49}$) of MERS-CoV M^{pro} (Figure 5C, left) that forms the S4 pocket.

In order to see the impact of inhibitor binding to these proteases, we employed differential scanning fluorimetry (DSF) to analyze the stabilization effect of the compound binding. We observed a drastic effect of ibuzatrelvir on melting temperatures (T_m) of both proteins. The increase in T_m in comparison to that of the apo form for SARS-CoV-2 M^{pro} was 16 °C (Figure S2C). Interestingly, for MERS-CoV M^{pro}, two peaks were detected in the presence of the inhibitor with 4 and 13 °C increases compared to the apo protease (Figure S2A,C). To check if this effect was unique for ibuzatrelvir binding, we performed the thermal shift assay for MERS-CoV M^{pro} after incubation with nirmatrelvir, which also demonstrated a bimodal melting curve with similar T_m values (Figure S2B,C). A possible explanation of a more complex melting profile may be the difference in dimerization between SARS-CoV-2 and MERS-CoV main proteases. As revealed in a previous study, MERS-CoV M^{pro} shows substrate-inducible dimerization.[31] The protein exists in monomeric form and

dimerizes upon substrate binding, and after the catalytic cycle, the dimers dissociate. In contrast, the dimerization of SARS-CoV-2 M^{pro} is not substrate-binding-dependent. The difference in behavior is defined by the difference in intermolecular interactions at the dimerization interface. MERS-CoV M^{pro} contains only two pairs of hydrogen bonds (Ser1-Glu169 and Ser142-Gln299), which bring two monomers together, as opposed to SARS-CoV-2 dimer featuring five amino acid pairs involved in the intermolecular interaction: Ser1-Glu166, Glu14-Gly11, Ser10-Ser10, Arg4-Glu290, and Gln299-Ser139. Two peaks on the melting profile of MERS-CoV M^{pro} complexed with ibuzatrelvir may reflect several situations. In order to gain insight into the oligomeric state of proteases during inhibition, we performed mass photometry analysis, which demonstrated that the oligomerization behavior was indeed different between SARS-CoV-2 and MERS-CoV M^{pro}s (Figure S4). The apo form of SARS-CoV-2 M^{pro} existed in solution primarily (73%) in dimeric form with only 27% being monomeric (Figure S4A,B). However, the apo form of MERS-CoV M^{pro} existed in solution mostly as monomers (98% of protein sample). Upon SARS-CoV-2 M^{pro} incubation with ibuzatrelvir, we observed inhibitor-induced dimerization, with 93% of the protein-inhibitor complex becoming dimeric, with an increased melting temperature (ΔT_m = 16 °C) (Figure S4B). For MERS-CoV M^{pro}, inhibitor addition triggered the formation of dimers (19%), but most of the protein (81%) still stayed in the monomeric form (Figure S4D). These data provide an explanation for the bimodal melting curve of MERS-CoV and M^{pro}. In the presence of ibuzatrelvir, the first

peak with a 4 °C increase in T_m represents denaturation of the ibuzatrelvir complex with monomers, and the inhibitor-bound dimers may have a more drastic, 13 °C increase in thermal stability (Figure S2B,C).

Despite the significant effect of drug binding on the proteins' stabilities, we did not observe major conformational changes between apo and inhibitor-bound structures for either protease. T_m shifts could be explained by the large number of hydrophobic interactions and hydrogen bonds with the inhibitor, which contribute to overall complex stability. The structural superimposition of SARS-CoV-2 M^{pro} in complex with ibuzatrelvir and apo SARS-CoV-2 M^{pro} (PDB: 6WTM, chain A) gave a Z-score of 47.7 and aligned 306 Cα atoms with a root-mean-square deviation (RMSD) of 0.4 Å, which indicates only a slight conformational change after drug binding (Figure 5A)—a slight widening of the S4 pocket in response to inhibitor binding. Interestingly, in the MERS-CoV M^{pro}, ibuzatrelvir induced rearrangement of the secondary structure of the loop involved in the S4 binding site. Two residues of the ${}_{170}\underline{LANGT}_{174}$ loop, Leu170 and Ala171, became a part of a nearby β-sheet, extending it and further stabilizing the S4 pocket (Figure 5B).

Duration of action is a very important parameter in drug development. Several factors influence duration of action, including metabolic stability, the activity of metabolites, and the reversibility of drug action. A recent paper described the improved metabolic stability and pharmacokinetics of ibuzatrelvir compared to nirmatrelvir with intrinsic clearance, $CL_{int,app}$ of 4.72 μL/min/μg for the former and 28.8 μL/min/μg for the latter.[14] In this study, we aimed to assess the reversibility of ibuzatrelvir. Even though reversibility and intrinsic clearance do not correlate, both of these parameters are important for a drug's action. Covalent drugs with low off-rates provide advantages such as increased residency time at the target molecule, which allows a decreased dosage and reduced frequency of administration. Indeed, for SARS-CoV-2 M^{pro} complexed with ibuzatrelvir, we observed a reactivation half-time ($t_{1/2}$) of 85 h, whereas for nirmatrelvir, $t_{1/2}$ value was shown to be 115 h (Figure 2C). Dissociation of ibuzatrelvir from MERS-CoV M^{pro} was faster and resulted in $t_{1/2}$ reactivation of 23 h, which could be explained by the described differences in substrate binding (Figure 2D).

Our lab previously characterized crystal structures and inhibition of several SARS-CoV-2 M^{pro} from variants of concern (VOCs).[29] Here, we tested ibuzatrelvir inhibition on the M^{pro} of SARS-CoV-2 VOCs that bear mutations located close to the binding site of the inhibitor (Figure S5A). For the δ-associated L50F variant, our crystal structure showed that the surface around the S2 pocket became more hydrophobic compared to the wild-type protein,[29] which in turn made the interactions with the P2 group of ibuzatrelvir more favorable, decreasing the IC_{50} value to 6 nM (Table 1). Residue Glu47, located in close proximity to the catalytic histidine and gateway loop in domain I, was found to have two substitutions with VOCs: to E47N in α SARS-CoV-2 VOCs and to E47K in all VOCs. These mutations led to changes in shape and charge of the S4 pocket.[29] With E47N, the strong negative charge of S4 increases the IC_{50} value for ibuzatrelvir about 2 times (Table 1), possibly by altering the interaction with hydrophobic P2 position of ibuzatrelvir. In contrast, E47K substitution did not affect the structure of the SARS-CoV-2 protease, and the IC_{50} value remained unchanged (Table 1). Another mutation located on the gateway loop but in domain II was T190I

(Figure S5A). This substitution was found in the α and δ SARS-CoV-2 variants. We previously showed that the structure of this mutant also remained unaltered,[29] and here we demonstrated that the IC_{50} of ibuzatrelvir did not change significantly (Table 1). Omicron variant mutation (P132H) and the S46F substitution in M^{pro} did not affect IC_{50} values for ibuzatrelvir as well. Together, these data demonstrate that ibuzatrelvir has a high potency against M^{pro} variants of SARS-CoV-2.

◼ DISCUSSION

It has been four years since the outbreak of SARS-CoV-2. Both vaccines (https://www.fda.gov/emergency-preparedness-and-response/coronavirus-disease-2019-covid-19/covid-19-vaccines-2023-2024) and small-molecule drugs[1,30] have been developed to prevent viral infection. Due to the high variation of SARS-CoV-2 spike protein, small-molecule inhibitors targeting conserved viral proteins are more likely to be effective against variants, making M^{pro} a key target for drug development. The first-generation antiviral drug Paxlovid demonstrated high efficacy against SARS-CoV-2 infection, despite some metabolic stability issues. However, the second-generation oral drug candidate ibuzatrelvir has overcome this problem. As reported in our previous paper,[18] two soft spots related to metabolic stability were identified in nirmatrelvir: the CH_3 group at P2 and next to the nitrogen at P1. The P2 group is more susceptible to metabolism. The CF3 alteration at the P2 group of ibuzatrelvir effectively prevents oxidation at this site, stabilizing the drug against clearance by the CYP enzymes. Additionally, this modification increases the binding efficiency to M^{pro} by generating electrostatic interactions.

Both nirmatrelvir and ibuzatrelvir are designed based on SARS-CoV-2 substrate specificities, since the inhibitor with a structure closer to the substrate will be preferentially recognized by M^{pro}, demonstrating higher inhibition potency. According to our study on the substrate specificity of SARS-CoV-2 M^{pro}, as well as M^{pro} of SARS-CoV-2 VOCs, leucine is favored at P2, while hydrophobic residues with small side chain, such as alanine and valine, are preferred at P4 since S4 pocket is small which can only accommodate residues with small side chains.[29] The substrate with alanine at P4, represented in the cleavage site between nsp4 and nsp5, demonstrated higher affinity to SARS-CoV-2 M^{pro} than the substrate with valine at P4, represented in the cleavage site between nsp5 and nsp6.[31] This explains the tight binding of ibuzatrelvir with an alanine derivative as its capping group to the SARS-CoV-2 M^{pro} active site.

Interestingly, despite highly similar binding patterns of ibuzatrelvir to active sites of M^{pro} from SARS-CoV-2 and MERS-CoV, the K_i value of ibuzatrelvir for SARS-CoV-2 M^{pro} is 6 times lower than for MERS-CoV M^{pro} (5 versus 31 nM respectively). Also, we observed a difference in the reversibility of compound for both proteases (85 vs 23 h). The S4 pocket of MERS-CoV M^{pro} is bigger than that of SARS-CoV-2 M^{pro}, and it is able to accommodate bulky amino acids, like tyrosine at the C-terminus of nsp13 within the $\underline{YKLQ}$ sequence (P4 to P1), in addition to hydrophobic residues with small side chains. The small methyl carbonate group of ibuzatrelvir does not occupy the pocket as efficiently as tyrosine. In contrast, SARS-CoV-2 S4 pocket favors only residues with small side chains, like alanine or valine. Thus, the S4 pocket of MERS-CoV M^{pro} is less susceptible to residue size than that of SARS-CoV-2 M^{pro}. This might explain the faster reversibility and

lower inhibition potency of ibuzatrelvir for the MERS-CoV M^{pro}.

Our results indicated that in both cases, the ibuzatrelvir reversibly forms a thioimidate active site covalent adduct. Reversibility of the thiol-warhead interaction is important to minimize destruction of the inhibitor by nonspecific reaction with mammalian thiols and also avoid possible human toxicity. The enzyme—inhibitor recognition features that help lock the ibuzatrelvir into both enzymes include hydrogen bonding of the P1 glutamine analogue side chain, the very tight fit of the trifluoromethyl group at P2 and the tight recognition of the methyl carbamate at P4. Additionally, we observed inhibitor-induced oligomerization with MERS-CoV M^{pro}, similar to previous substrate-induced dimerization studies.[23]

Recently, new SARS-CoV-2 variants, classified as variants of interest (VOIs), have been identified. For example, strain JN.1.11, prevalent in North America and globally, has mutations in the Spike protein but only the P132H mutation in M^{pro} (https://covid.cdc.gov/covid-data-tracker/#variant-proportions). Fortunately, ibuzatrelvir demonstrated high inhibition potency on variants of concern of SARS-CoV-2, likely due to the conservation of active site machinery, which together with MERS-CoV M^{pro} results suggests that ibuzatrelvir may prove to be effective against many coronaviral infections. However, the potential emergence of drug-resistant strains should be paid attention to, as the nirmatrelvir resistance mutations have been found in M^{pro} such as E166V, L50F, and a combination of them.[32−34]

■ MATERIALS AND METHODS

Protein Expression and Purification

The SARS-CoV-2 M^{pro} (GenBank: MN908947.3) was expressed in *Escherichia coli* BL21 (DE3) as described earlier.[9] MERS-CoV M^{pro} (GenBank: AGV08401.1) was expressed similarly. Briefly, the *E. coli* codon usage optimized gene was inserted into pET-SUMO expression vector (Invitrogen), containing an N-terminal hexa-His tag followed by SUMO tag. The plasmid was transformed into *E. coli* BL21 (DE3) competent cells. Protein expression was induced with 0.3 mM isopropyl β-D-1-thiogalactopyranoside (IPTG) and expressed at 18 °C for ~16 h. The cell pellets were resuspended with buffer A containing 50 mM tris(hydroxymethyl)aminomethane (Tris) pH 8.0, 300 mM NaCl, 20 mM imidazole, and 2 mM β-mercaptoethanol (β-ME) buffer and then lysed using Emulsiflex. The lysate was cleared by centrifugation at 18,000g for 60 min at 4 °C, and then the supernatant was loaded onto Ni-NTA column (Qiagen, Canada). The protein of interest was eluted with 50 mM Tris pH 8.0, 300 mM NaCl, and 300 mM imidazole. The His-SUMO tag was cleaved with the His-tagged SUMO protease Ulp1 (McLab, South San Francisco, CA) during dialysis. The His-SUMO tag and Ulp1 were removed with Ni-NTA column, tag removed protein was collected and concentrated for gel filtration, and protein was loaded on Superdex 200 increase 10/300 column (Cytiva, Canada) equilibrated with a gel filtration buffer containing 20 mM Tris pH 8.0, 100 mM NaCl, 1 mM TCEP. Fractions containing pure main protease were pooled and concentrated to 8 mg/mL. Protein was aliquoted, flash-frozen, and stored at −80 °C.

Crystallization, Data Processing, and Structure Determination

The crystals of SARS-CoV-2 M^{pro} in complex with ibuzatrelvir were obtained by soaking. Apo SARS-CoV-2 main protease was crystallized at 18 °C in a sitting drop by mixing 2 μL of protein and 2 μL of crystallization buffer containing 0.22 M Ammonium chloride, 0.1 M HEPES pH 7.0, 22% PEG 6,000 manually. Crystals appeared after 3 days. Best crystals were soaked with ibuzatrelvir by adding 2 μL of 10, 5, 2.5 mM inhibitor to the drop for 3 and 16 h. The crystals then were

flash-frozen in liquid nitrogen after being passed through 20% glycerol as a cryoprotectant. The crystals of MERS-CoV main protease in complex with ibuzatrelvir were obtained by cocrystallization. 1 mg/mL of protein was incubated with 5 molar access of ibuzatrelvir at 4 °C overnight, and the complex was concentrated to ~10 mg/mL. Crystallization conditions were screened by using a Phoenix ARI crystallization Robot (Art Robbins Instruments), crystals appeared in 3 days. The data was collected at Stanford Synchrotron Radiation Lightsource (SSRL), at beamline 12−1. The data was processed using XDS program.[35] For SARS-CoV-2 M^{pro} in complex with ibuzatrelvir, the molecular placement was done by CCP4 phaser MR[36,37] program using an apo SARS-CoV-2 M^{pro} structure (PDB: 6WTM) as a search model. For MERS-CoV M^{pro} in complex with ibuzatrelvir, apo structure (PDB: 5C3N) was used as a search model for molecular replacement by CCP4 phaser MR program.[36,37] Ligand was fit using Phenix.ligand.fit program.[38,39] Structure refined using Phenix[40] and modified manually in Coot.[41] Data statistics are summarized in Table S1.

Differential Scanning Fluorimetry

DFS was performed using 8 μM protease with a final concentration of 5× for SYBR Orange dye (Thermo Fisher Scientific) in 20 mM Tris-HCl, pH 8.0, 150 mM NaCl buffer. All samples were run in duplicate. The thermal scan was conducted from 4 to 95 °C, at a resolution of 0.05 °C/s (Quantstudio 5, Thermo Fisher). The melting point (T_m) was calculated by fitting the raw fluorescence data over the temperature using the Boltzmann equation, and the data was analyzed by Protein Thermal Shift Software Version 1.3.

FRET-Based M^{pro} Activity and Inhibition Assays

FRET-based cleavage assays with the synthesized fluorescent substrate of SARS-CoV-2 M^{pro} (Abz-SVTLQ↓SG-Tyr(NO2)-R) were conducted as described previously.[10] For the determination of the IC$_{50}$ values, 100 nM SARS-CoV-2 M^{pro} and 400 nM MERS-CoV M^{pro} were incubated with ibuzatrelvir at various concentrations from 0 to 400 μM in 20 mM Bis-Tris, pH 7.4, 1 mM DTT for 10 min. The protease reaction was started by the addition of 100 μM of the substrate. The GraphPad Prism software (GraphPad 8.3.1) was used for the calculation of the IC$_{50}$ values. For K_i determination, 100 nM SARS-CoV-2 M^{pro} and 400 nM MERS-CoV ^{Mpro} were preincubated with ibuzatrelvir in the concentration range of 0.01−0.4 μM for 10 min at 37 °C. The enzymatic reactions using 1−500 μM FRET substrate in activity buffer (25 mM Bis-Tris, 1 mM DTT, pH 7.4) were started with the addition of protease and monitored at an emission wavelength of 420 nm with excitation at 320 nm, using a Cytation 5 Imaging Multi-Mode Reader (BioTek) for 7 min at 37 °C. The kinetic data were analyzed using computer-fit calculation (Prism 9.0, GraphPad Software).

Reversibility Studies

Reversibility studies were performed using dialysis. 3 μM SARS-CoV-2 and MERS-CoV M^{pro} samples were incubated with 20 μM ibuzatrelvir as the final concentration for 10 min. The compound was dissolved in DMSO. The protease samples incubated with DMSO at the same concentration (1%) were used as a control. After demonstrating the full inhibition of protease activities, the samples were put on dialysis against 50 mM Tris-HCl, pH 7.4, 200 mM NaCl, 5% glycerol, and 1 mM DTT for 72 h at room temperature. The dialysis buffer was changed every 3−6 h to ensure that dissociated drug is diluted to a negligible concentration. The aliquots were taken at specific time points, and M^{pro} activity was measured using a FRET-based assay.

Mass Photometry

All mass photometry measurements were acquired using a Refeyn OneMP mass photometer with Refeyn Acquire MP software. M^{pro}'s were diluted in a buffer containing 25 mM Tris-HCl pH 8.0, 100 mM NaCl, and 2 mM TCEP to 1 mg/mL. Ibuzatrelvir (200 mM in DMSO) was added to the M^{pro} sample with 5 molar access, and the complex was incubated at 4 °C for 1 h. DMSO alone was added to M^{pro} at the same concentration, and the sample was used as a negative

control. After incubation, the proteins were diluted 200 times in the same buffer (0.005 mg/mL) before being applied to a microscope slide (Thorlabs High Precision Microscope Cover Glasses 25 mm × 50 mm, 170 μM, No. 1.5H). The mass photometer was calibrated using BSA solution with 3 oligomers: monomer (66.5 kDa), dimer (133.0 kDa), tetramer (266.0 kDa). After calibration, 1 μL of protein (0.005 mg/mL) was mixed with 19 μL of buffer on the microscope slide thoroughly, the protein sample was screened and recorded for 1 min by the software Refeyn Discover^{MP}, and the results were exported for further analysis. Refeyn EVALUATE^{MP} was used to analyze the data.

ASSOCIATED CONTENT

Data Availability Statement

All data are available in the main text or the Supporting Information. Inhibitors are available with materials transfer agreements (MTAs). Structural data has been deposited in the www.rscb.org database with accession numbers: 9BPF, 9BOO.

Supporting Information

The Supporting Information is available free of charge at https://pubs.acs.org/doi/10.1021/jacsau.4c00508.

> Data collection and refinement statistics (Table S1); overall crystal structure of MERS-CoV M^{pro} and SARS-CoV-2 M^{pro} (Figure S1); DSF melt curves (Figure S2); dose-response curves (Figure S3); oligomerization of the M^{pro} enzymes (Figure S4); residues around the active site of the SARS-CoV-2 M^{pro} (Figure S5); synthetic route to ibuzatrelvir (Figure S6); HPLC chromatograms (Figure S7); ^{1}H NMR spectrum (Figure S8), and GC chromatogram (Figure S9) (PDF)

AUTHOR INFORMATION

Corresponding Authors

John C. Vederas − *Department of Chemistry, University of Alberta, Edmonton, Alberta T6G 2G2, Canada;* ⊙ orcid.org/0000-0002-2996-0326; Email: john.vederas@ualberta.ca

M. Joanne Lemieux − *Department of Biochemistry, University of Alberta, Edmonton, Alberta T6G 2H7, Canada; Li Ka Shing Institute of Virology, University of Alberta, Edmonton, Alberta T6G 2E1, Canada;* ⊙ orcid.org/0000-0003-4745-9153; Email: mlemieux@ualberta.ca

Authors

Pu Chen − *Department of Biochemistry, University of Alberta, Edmonton, Alberta T6G 2H7, Canada; Li Ka Shing Institute of Virology, University of Alberta, Edmonton, Alberta T6G 2E1, Canada*

Tayla J. Van Oers − *Department of Chemistry, University of Alberta, Edmonton, Alberta T6G 2G2, Canada;* ⊙ orcid.org/0009-0006-2314-560X

Elena Arutyunova − *Department of Biochemistry, University of Alberta, Edmonton, Alberta T6G 2H7, Canada; Li Ka Shing Institute of Virology, University of Alberta, Edmonton, Alberta T6G 2E1, Canada;* ⊙ orcid.org/0000-0003-4119-3622

Conrad Fischer − *Department of Chemistry, University of Alberta, Edmonton, Alberta T6G 2G2, Canada;* ⊙ orcid.org/0000-0002-2289-010X

Chaoxiang Wang − *Department of Chemistry, University of Alberta, Edmonton, Alberta T6G 2G2, Canada*

Tess Lamer − *Department of Chemistry, University of Alberta, Edmonton, Alberta T6G 2G2, Canada;* ⊙ orcid.org/0000-0002-1511-4540

Marco J. van Belkum − *Department of Chemistry, University of Alberta, Edmonton, Alberta T6G 2G2, Canada;* ⊙ orcid.org/0000-0002-9296-6069

Howard S. Young − *Department of Biochemistry, University of Alberta, Edmonton, Alberta T6G 2H7, Canada;* ⊙ orcid.org/0000-0002-5990-8422

Complete contact information is available at:
https://pubs.acs.org/10.1021/jacsau.4c00508

Author Contributions

Conceptualization: P.C., T.J.V.O., E.A., J.V., M.J.L. Methodology: P.C., T.J.V.O., E.A., C.F., C.W., T.L., J.C.V., M.J.L. Investigation: P.C., T.J.V.O., E.A., C.F., C.W., T.L., M.J.v.B. Visualization: T.J.V.O., P.C., E.A., J.C.V., M.J.L. Supervision: H.S.Y., J.C.V., M.J.L. Writing: P.C., T.J.V.O., E.A., J.C.V., M.J.L. Writing—review and editing: P.C., E.A., T.J.V.O., C.F., C.W., T.L., M.J.v.B., H.S.Y., J.C.V., M.J.L. The manuscript was written through contributions of all authors. All authors have given approval to the final version of the manuscript.

Notes

The authors declare no competing financial interest.

and the University of Saskatchewan. T.L. was supported by a Vanier Canada Graduate Scholarship (CIHR).

■ ABBREVIATIONS

M^pro   main protease

■ REFERENCES

(1) Owen, D. R.; Allerton, C. M. N.; Anderson, A. S.; Aschenbrenner, L.; Avery, M.; Berritt, S.; Boras, B.; Cardin, R. D.; Carlo, A.; Coffman, K. J.; et al. An oral SARS-CoV-2 M(pro) inhibitor clinical candidate for the treatment of COVID-19. *Science* **2021**, *374* (6575), 1586−1593.

(2) Beigel, J. H.; Tomashek, K. M.; Dodd, L. E.; Mehta, A. K.; Zingman, B. S.; Kalil, A. C.; Hohmann, E.; Chu, H. Y.; Luetkemeyer, A.; Kline, S.; et al. Remdesivir for the Treatment of Covid-19 - Final Report. *N. Engl. J. Med.* **2020**, *383* (19), 1813−1826.

(3) Jiang, X.; Su, H.; Shang, W.; Zhou, F.; Zhang, Y.; Zhao, W.; Zhang, Q.; Xie, H.; Jiang, L.; Nie, T.; et al. Structure-based development and preclinical evaluation of the SARS-CoV-2 3C-like protease inhibitor simnotrelvir. *Nat. Commun.* **2023**, *14* (1), No. 6463.

(4) Mackman, R. L.; Kalla, R. V.; Babusis, D.; Pitts, J.; Barrett, K. T.; Chun, K.; Du Pont, V.; Rodriguez, L.; Moshiri, J.; Xu, Y.; et al. Discovery of GS-5245 (Obeldesivir), an Oral Prodrug of Nucleoside GS-441524 That Exhibits Antiviral Efficacy in SARS-CoV-2-Infected African Green Monkeys. *J. Med. Chem.* **2023**, *66* (17), 11701−11717.

(5) Mukae, H.; Yotsuyanagi, H.; Ohmagari, N.; Doi, Y.; Sakaguchi, H.; Sonoyama, T.; Ichihashi, G.; Sanaki, T.; Baba, K.; Tsuge, Y.; Uehara, T. Efficacy and Safety of Ensitrelvir in Patients With Mild-to-Moderate Coronavirus Disease 2019: The Phase 2b Part of a Randomized, Placebo-Controlled, Phase 2/3 Study. *Clin. Infect. Dis.* **2023**, *76* (8), 1403−1411.

(6) Brunetti, L.; Diawara, O.; Tsai, A.; Firestein, B. L.; Nahass, R. G.; Poiani, G.; Schlesinger, N. Colchicine to Weather the Cytokine Storm in Hospitalized Patients with COVID-19. *J. Clin. Med.* **2020**, *9* (9), No. 2961.

(7) Monteil, V.; Kwon, H.; Prado, P.; Hagelkruys, A.; Wimmer, R. A.; Stahl, M.; Leopoldi, A.; Garreta, E.; Del Pozo, C. H.; Prosper, F.; et al. Inhibition of SARS-CoV-2 Infections in Engineered Human Tissues Using Clinical-Grade Soluble Human ACE2. *Cell* **2020**, *181* (4), 905−913.

(8) Gupta, D.; Sahoo, A. K.; Singh, A. Ivermectin: potential candidate for the treatment of Covid 19. *Braz. J. Infect. Dis.* **2020**, *24* (4), 369−371.

(9) Bege, M.; Borbas, A. The Design, Synthesis and Mechanism of Action of Paxlovid, a Protease Inhibitor Drug Combination for the Treatment of COVID-19. *Pharmaceutics* **2024**, *16* (2), No. 217.

(10) Vuong, W.; Khan, M. B.; Fischer, C.; Arutyunova, E.; Lamer, T.; Shields, J.; Saffran, H. A.; McKay, R. T.; van Belkum, M. J.; Joyce, M. A.; et al. Feline coronavirus drug inhibits the main protease of SARS-CoV-2 and blocks virus replication. *Nat. Commun.* **2020**, *11* (1), No. 4282.

(11) Chary, M.; Barbuto, A. F.; Izadmehr, S.; Tarsillo, M.; Fleischer, E.; Burns, M. M. COVID-19 Therapeutics: Use, Mechanism of Action, and Toxicity (Vaccines, Monoclonal Antibodies, and Immunotherapeutics). *J. Med. Toxicol.* **2023**, *19* (2), 205−218.

(12) Ross, S. B.; Bortolussi-Courval, E.; Hanula, R.; Lee, T. C.; Wilson, M. G.; McDonald, E. G. Drug Interactions With Nirmatrelvir-Ritonavir in Older Adults Using Multiple Medications. *JAMA Network Open* **2022**, *5* (7), No. e2220184.

(13) Ducharme, J.; Sevrioukova, I. F.; Thibodeaux, C. J.; Auclair, K. Structural Dynamics of Cytochrome P450 3A4 in the Presence of Substrates and Cytochrome P450 Reductase. *Biochemistry* **2021**, *60* (28), 2259−2271.

(14) Allerton, C. M. N.; Arcari, J. T.; Aschenbrenner, L. M.; Avery, M.; Bechle, B. M.; Behzadi, M. A.; Boras, B.; Buzon, L. M.; Cardin, R. D.; Catlin, N. R.; et al. A Second-Generation Oral SARS-CoV-2 Main Protease Inhibitor Clinical Candidate for the Treatment of COVID-19. *J. Med. Chem.* **2024**, DOI: 10.1021/acs.jmedchem.3c02469.

(15) Zhao, Y.; Fang, C.; Zhang, Q.; Zhang, R.; Zhao, X.; Duan, Y.; Wang, H.; Zhu, Y.; Feng, L.; Zhao, J.; et al. Crystal structure of SARS-CoV-2 main protease in complex with protease inhibitor PF-07321332. *Protein Cell* **2022**, *13* (9), 689−693.

(16) La Monica, G.; Bono, A.; Lauria, A.; Martorana, A. Targeting SARS-CoV-2 Main Protease for Treatment of COVID-19: Covalent Inhibitors Structure-Activity Relationship Insights and Evolution Perspectives. *J. Med. Chem.* **2022**, *65* (19), 12500−12534.

(17) Kneller, D. W.; Li, H.; Phillips, G.; Weiss, K. L.; Zhang, Q.; Arnould, M. A.; Jonsson, C. B.; Surendranathan, S.; Parvathareddy, J.; Blakeley, M. P.; et al. Covalent narlaprevir- and boceprevir-derived hybrid inhibitors of SARS-CoV-2 main protease. *Nat. Commun.* **2022**, *13* (1), No. 2268.

(18) Arutyunova, E.; Belovodskiy, A.; Chen, P.; Khan, M. B.; Joyce, M.; Saffran, H.; Lu, J.; Turner, Z.; Bai, B.; Lamer, T.; et al. The Effect of Deuteration and Homologation of the Lactam Ring of Nirmatrelvir on Its Biochemical Properties and Oxidative Metabolism. *ACS Bio Med. Chem. Au* **2023**, *3* (6), 528−541.

(19) Bai, B.; Arutyunova, E.; Khan, M. B.; Lu, J.; Joyce, M. A.; Saffran, H. A.; Shields, J. A.; Kandadai, A. S.; Belovodskiy, A.; Hena, M.; et al. Peptidomimetic nitrile warheads as SARS-CoV-2 3CL protease inhibitors. *RSC Med. Chem.* **2021**, *12* (10), 1722−1730.

(20) Toussi, S. S.; Hammond, J. L.; Gerstenberger, B. S.; Anderson, A. S. Therapeutics for COVID-19. *Nat. Microbiol.* **2023**, *8* (5), 771−786.

(21) Zhang, L.; Lin, D.; Sun, X.; Curth, U.; Drosten, C.; Sauerhering, L.; Becker, S.; Rox, K.; Hilgenfeld, R. Crystal structure of SARS-CoV-2 main protease provides a basis for design of improved alpha-ketoamide inhibitors. *Science* **2020**, *368* (6489), 409−412.

(22) Vuong, W.; Fischer, C.; Khan, M. B.; van Belkum, M. J.; Lamer, T.; Willoughby, K. D.; Lu, J.; Arutyunova, E.; Joyce, M. A.; Saffran, H. A.; et al. Improved SARS-CoV-2 M(pro) inhibitors based on feline antiviral drug GC376: Structural enhancements, increased solubility, and micellar studies. *Eur. J. Med. Chem.* **2021**, *222*, No. 113584.

(23) Arutyunova, E.; Khan, M. B.; Fischer, C.; Lu, J.; Lamer, T.; Vuong, W.; van Belkum, M. J.; McKay, R. T.; Tyrrell, D. L.; Vederas, J. C.; et al. N-Terminal Finger Stabilizes the S1 Pocket for the Reversible Feline Drug GC376 in the SARS-CoV-2 M(pro) Dimer. *J. Mol. Biol.* **2021**, *433* (13), No. 167003.

(24) Van Oers, T. J.; Piercey, A.; Belovodskiy, A.; Reiz, B.; Donnelly, B. L.; Vuong, W.; Lemieux, M. J.; Nieman, J. A.; Auclair, K.; Vederas, J. C. Deuteration for Metabolic Stabilization of SARS-CoV-2 Inhibitors GC373 and Nirmatrelvir. *Org. Lett.* **2023**, *25* (31), 5885−5889.

(25) Del Valle, J. R.; Goodman, M. Stereoselective synthesis of Boc-protected cis and trans-4-trifluoromethylprolines by asymmetric hydrogenation reactions. *Angew. Chem., Int. Ed.* **2002**, *41* (9), 1600−1602.

(26) Ghosh, A. K.; Yadav, M. Synthesis of optically active SARS-CoV-2 Mpro inhibitor drug nirmatrelvir (Paxlovid): an approved treatment of COVID-19. *Org. Biomol. Chem.* **2023**, *21* (28), 5768−5774.

(27) Wedemeyer, W. J.; Welker, E.; Scheraga, H. A. Proline cis-trans isomerization and protein folding. *Biochemistry* **2002**, *41* (50), 14637−14644.

(28) Krissinel, E.; Henrick, K. Inference of macromolecular assemblies from crystalline state. *J. Mol. Biol.* **2007**, *372* (3), 774−797.

(29) Chen, S. A.; Arutyunova, E.; Lu, J.; Khan, M. B.; Rut, W.; Zmudzinski, M.; Shahbaz, S.; Iyyathurai, J.; Moussa, E. W.; Turner, Z.; et al. SARS-CoV-2 M(pro) Protease Variants of Concern Display Altered Viral Substrate and Cell Host Target Galectin-8 Processing but Retain Sensitivity toward Antivirals. *ACS Cent. Sci.* **2023**, *9* (4), 696−708.

(30) Fischer, W. A., 2nd; Eron, J. J., Jr.; Holman, W.; Cohen, M. S.; Fang, L.; Szewczyk, L. J.; Sheahan, T. P.; Baric, R.; Mollan, K. R.; Wolfe, C. R.; et al. A phase 2a clinical trial of molnupiravir in patients with COVID-19 shows accelerated SARS-CoV-2 RNA clearance and

elimination of infectious virus. *Sci. Transl. Med.* **2022**, *14* (628), No. eabl7430.

(31) Zhao, Y.; Zhu, Y.; Liu, X.; Jin, Z.; Duan, Y.; Zhang, Q.; Wu, C.; Feng, L.; Du, X.; Zhao, J.; et al. Structural basis for replicase polyprotein cleavage and substrate specificity of main protease from SARS-CoV-2. *Proc. Natl. Acad. Sci. U.S.A.* **2022**, *119* (16), No. e2117142119.

(32) Kiso, M.; Furusawa, Y.; Uraki, R.; Imai, M.; Yamayoshi, S.; Kawaoka, Y. In vitro and in vivo characterization of SARS-CoV-2 strains resistant to nirmatrelvir. *Nat. Commun.* **2023**, *14* (1), No. 3952.

(33) Zhou, Y.; Gammeltoft, K. A.; Ryberg, L. A.; Pham, L. V.; Tjornelund, H. D.; Binderup, A.; Duarte Hernandez, C. R.; Fernandez-Antunez, C.; Offersgaard, A.; Fahnoe, U.; et al. Nirma-trelvir-resistant SARS-CoV-2 variants with high fitness in an infectious cell culture system. *Sci. Adv.* **2022**, *8* (51), No. eadd7197.

(34) Lan, S.; Neilsen, G.; Slack, R. L.; Cantara, W. A.; Castaner, A. E.; Lorson, Z. C.; Lulkin, N.; Zhang, H.; Lee, J.; Cilento, M. E. et al. Nirmatrelvir Resistance in SARS-CoV-2 Omicron_BA.1 and WA1 Replicons and Escape Strategies *bioRxiv* 2023, DOI: 10.1101/2022.12.31.522389.

(35) Kabsch, W. Integration, scaling, space-group assignment and post-refinement. *Acta Crystallogr., Sect. D: Biol. Crystallogr.* **2010**, *66* (Pt 2), 133−144.

(36) McCoy, A. J.; Grosse-Kunstleve, R. W.; Adams, P. D.; Winn, M. D.; Storoni, L. C.; Read, R. J. Phaser crystallographic software. *J. Appl. Crystallogr.* **2007**, *40* (Pt 4), 658−674.

(37) Agirre, J.; Atanasova, M.; Bagdonas, H.; Ballard, C. B.; Basle, A.; Beilsten-Edmands, J.; Borges, R. J.; Brown, D. G.; Burgos-Marmol, J. J.; Berrisford, J. M.; et al. The CCP4 suite: integrative software for macromolecular crystallography. *Acta Crystallogr., Sect. D: Biol. Crystallogr.* **2023**, *79* (Pt 6), 449−461.

(38) Terwilliger, T. C.; Adams, P. D.; Moriarty, N. W.; Cohn, J. D. Ligand identification using electron-density map correlations. *Acta Crystallogr., Sect. D: Biol. Crystallogr.* **2007**, *63* (Pt 1), 101−107.

(39) Terwilliger, T. C.; Klei, H.; Adams, P. D.; Moriarty, N. W.; Cohn, J. D. Automated ligand fitting by core-fragment fitting and extension into density. *Acta Crystallogr., Sect. D: Biol. Crystallogr.* **2006**, *62* (Pt 8), 915−922.

(40) Adams, P. D.; Afonine, P. V.; Bunkoczi, G.; Chen, V. B.; Davis, I. W.; Echols, N.; Headd, J. J.; Hung, L. W.; Kapral, G. J.; Grosse-Kunstleve, R. W.; et al. PHENIX: a comprehensive Python-based system for macromolecular structure solution. *Acta Crystallogr., Sect. D: Biol. Crystallogr.* **2010**, *66* (Pt 2), 213−221.

(41) Emsley, P.; Lohkamp, B.; Scott, W. G.; Cowtan, K. Features and development of Coot. *Acta Crystallogr., Sect. D: Biol. Crystallogr.* **2010**, *66* (Pt 4), 486−501.